**Theoretical and Computational
Fluid Dynamics**

Noise Investigation of a High Subsonic,
Moderate Reynolds Number Jet Using a Compressible Large
Eddy Simulation*

C. Bogey, C. Bailly, and D. Juvé

LMFA, UMR CNRS 5509, Ecole Centrale de Lyon,
69134 Ecully, France

Abstract. This study investigates the noise radiated by a subsonic circular jet with a Mach number of 0.9 and a Reynolds number of 65 000 computed by a compressible Large Eddy Simulation (LES). First, it demonstrates the feasibility of using LES to predict accurately both the flow field and the sound radiation on a domain including the acoustic field. Mean flow parameters, turbulence intensities, velocity spectra and integral length scales are in very good agreement with experimental data. The noise generated by the jet, provided directly by the simulation, is also consistent with measurements in terms of sound pressure spectra, levels and directivity. The apparent location of the sound sources is at the end of the potential core in accordance with some experimental observations at similar Reynolds numbers and Mach numbers. Second, the noise generation mechanisms are discussed in an attempt to connect the flow field with the acoustic field. This study shows that for the simulated moderate Reynolds number jet, the predominant sound radiation in the downstream direction is associated with the breakdown of the shear layers in the central jet zone.

1. Introduction

1.1. Jet Noise

The early investigations on jet noise were performed in the framework of the acoustic analogy formulated by Lighthill (1952), where the noise generated by the region occupied by the turbulent flow, radiating over large distances, is regarded as a solution of the inhomogeneous wave equation in a medium at rest. The analogy was reformulated by Lilley (1972) and others to provide an appropriate expression for the sound sources, by incorporating the effects of mean flow on sound propagation into the wave operator. An important result of the analogy is to supply the dimensional law of the radiated acoustical power as a function of the jet velocity U_j, the famous U_j^8 law for subsonic jets. Pragmatic applications of the acoustic analogy to predict jet noise from a statistical description of turbulence have been derived since the works of Ribner (1964). They give global acoustic quantities such as the overall sound power in good agreement with experimental results, as

---

illustrated in Lilley (1996) or in Bailly *et al.* (1997). Applications using unsteady turbulence have been also proposed, see for instance the numerical study of Bastin *et al.* (1997). The acoustic analogy is appropriate for predicting jet noise when a sufficiently accurate solution of the turbulent flow is available.

The initial jet development, as well as the range of small scales, depends appreciably on the Reynolds number. This implies that the noise sources are necessarily modified as the Reynolds number varies. However, the presence of coherent turbulent structures was shown in experimental observations by Winant and Browand (1974) and by Brown and Roshko (1974), even at high Reynolds numbers, which raised questions of the possible predominant role of these large structures in jet noise generation. Thus, in supersonic jets, it is now well established, as presented in the paper of Tam (1995a), that the large scales are responsible for Mach wave radiation. Experiments of Troutt and McLaughlin (1982) have demonstrated that this radiation dominates the sound field, and, from a modeling point of view, Tam and Burton (1984) have used a matched asymptotic expansion method from an instability wave solution to an acoustic wave solution to explain the basic mechanism.

In subsonic jets, the respective role of large and small scales in the noise generation process has been a matter of debate for a long time. The similarities between radiations measured by Mollo-Christensen *et al.* (1964) and Stromberg *et al.* (1980) on subsonic jets with the same Mach number $M = 0.9$, but very different Reynolds numbers, suggest that sound generation in subsonic jets can be mainly attributed to coherent structures in the principal direction of radiation, i.e. around an angle of 30° to the downstream axis. Small-scale turbulence would then appear as a secondary noise source. Nevertheless, experiments conducted by Zaman (1985) on excited jets have shown that the sound generation is dependent on the laminar or turbulent initial shear layers, and therefore on the Reynolds number. On that controversial subject of subsonic jet noise mechanisms, new investigations are fortunately made possible by the direct calculation of the acoustic field.

1.2. Direct Calculation of the Acoustic Field

In this approach, the aerodynamic field and the acoustic field are provided in a single computation, by solving the compressible unsteady Navier–Stokes equations. In this way the computed acoustic field is *a priori* exact because no acoustic model is used. However, to compute the noise directly from the compressible flow motion equations, some issues of Computational AeroAcoustics (CAA) clearly presented by Tam (1995b) must be taken into account. In particular, appropriate numerical techniques, such as non-reflecting boundary conditions and schemes preserving the non-dispersive feature of acoustic waves, must be used to face the great disparity of level and length scale between the acoustics and the flow field.

Three methods can be used to solve the Navier–Stokes equations: Direct Numerical Simulation (DNS), Large Eddy Simulation (LES) and simulation of the Reynolds Averaged Navier–Stokes (RANS) equations. The Direct Numerical Simulation (DNS) approach consists of computing all turbulent scales down to the dissipating eddies. The first applications of DNS to compute noise for three-dimensional flows were performed by Freund *et al.* (2000) and Freund (2001) on supersonic and subsonic round jets respectively, with $Re_D = 3600$ for the subsonic jet. In Large Eddy Simulation (LES), only the larger scales are resolved while the effects of smaller unresolved ones are taken into account by a subgrid scale model. LES has been applied by Gamet and Estivalezes (1998) to obtain the acoustic near field radiated by a supersonic jet, in combination with a Kirchhoff surface method to propagate sound to the far field. It has also been used by Morris *et al.* (1999) to compute the radiation of a supersonic rectangular jet. More recently, it has been used by Zhao *et al.* (2001) and by Constantinescu and Lele (2001) for subsonic circular jets. Finally, unsteady Reynolds Averaged Navier–Stokes (RANS) equations using turbulence closures have also been used. This approach can be regarded as a very large eddy simulation where only the very large structures are resolved. It is limited to specific cases such as the computation of screech noise in supersonic jets. A well-documented example is provided by Shen and Tam (1998).

Among the different methods, LES appears as the most interesting one to approach a wide class of flows, since it is not restricted to very low Reynolds numbers as DNS, and, unlike the unsteady RANS simulations, an important part of the small scales can be accurately calculated, if properly accounted for by the grid resolution. The noise generated by the unresolved part of the small scales will be neglected. This noise is likely to be significant only for high frequencies, and it would be possible to take it into account through modeling using a statistical approach. The application of LES for the computation of jet noise is also justified by two experimental observations. First, the contributions of coherent structures and of the larger small scales may

be predominant. Second, the region between the nozzle exit and the end of the potential core, where flow events such as vortex pairings or laminar–turbulent transition take place, is of importance in the noise generation, and this region is intended to be well described by LES. Finally, it should be noted that the broadening of the acoustic spectra, and consequently of the part neglected by LES, will depend on the choice of the jet Reynolds number.

1.3. Present Investigation

In the present work, a circular jet with a Mach number $M_j = U_j/c_0 = 0.9$ and a Reynolds number of $Re_D = U_j D/\nu = 65\,000$ (c_0 is the ambient sound speed, D is the jet diameter, ν is the kinematic viscosity) is computed by LES. The numerical algorithm used is the three-dimensional extension of the one developed by Bogey *et al.* (2000) to study the noise generated by vortex pairings in a mixing layer. The first goal of the present work is to show the feasibility of the direct calculation of the noise radiated by a subsonic jet using a compressible LES. This feasibility will be checked by comparisons with available experimental data. Since a direct sound computation provides both the turbulent flow and its radiated sound field, comparisons will be done on these two aspects. The second goal is to extend our knowledge of noise generation mechanisms. In particular, great attention will be turned to the complex region at the end of the potential core where turbulent structures merge. Connections between the dynamics of the turbulent flow and the radiated sound field will be reported.

The choice of this Mach number of 0.9 is justified by the amount of experimental studies available in the literature, providing both aerodynamic results with Lau *et al.* (1979), and acoustic results with Mollo-Christensen *et al.* (1964), Lush (1971) and Stromberg *et al.* (1980). A DNS was moreover recently performed by Freund (2001) for a Reynolds number 3600 jet precisely at this Mach number, and has directly provided a radiated sound field in good agreement with experiments at very low Reynolds numbers. In the present LES, the jet Reynolds number of 65 000 has been chosen to be higher than those affordable by DNS, since it is the basic motivation of LES to deal with high Reynolds number flows. However, it is still quite inferior to the threshold of about 5×10^5 beyond which the shear layer is fully turbulent at the jet nozzle exit. For this reason, we expect to find an acoustic field and sound sources rather similar to those of a low Reynolds number jet.

The paper is organized as follows. The numerical procedure and parameters, as well as the inflow conditions, are presented in Section 2. The aerodynamic characteristics computed from the jet flow are studied in Section 3. They deal first with the laminar transition in the shear layers and second with the developed turbulent jet further downstream in the self-similar region. Turbulence intensities, velocity spectra, two point correlation functions and integral length scales are described, and validated by comparison with available measurements. In Section 4 the sound field generated by the jet flow is checked very carefully in terms of sound pressure levels and directivity. In addition, the spectral content of acoustic signals is analyzed with respect to the cut-off introduced by the spatial discretization. Validations making use of several sets of experimental data are extensively conducted. Section 5 is devoted to a display of the links between the dynamics of turbulent structures at the end of the potential core and the sound field emitted by the jet. To support this, a space–time analysis is developed to correlate intermittency of vorticity in the potential core with wave fronts propagating at low angles in the downstream direction.

2. Flow Simulation

2.1. Numerical Algorithm

LES is performed by solving the filtered three-dimensional Navier–Stokes equations provided in Appendix A. A model is required for the subgrid scale terms associated with the unresolved structures, and, considering that small-scale turbulence has mainly dissipative effects, the standard Smagorinsky turbulent viscosity is implemented.

The numerical algorithm developed to compute propagation problems using the linearized Euler equations in Bailly and Juvé (2000) and Bogey *et al.* (2002) is chosen. It has also previously been applied to

solve the two-dimensional Navier–Stokes equations in Bogey (2000). The seven-point stencil, Dispersion-Relation-Preserving (DRP) finite-difference scheme of Tam and Webb (1993) is used to discretize the spatial derivatives of the Euler fluxes. The coefficients of the DRP scheme are chosen to minimize errors on the effective wave number. In this way, this scheme introduces very low dispersion, with typically seven points required per wavelength. Euler fluxes are advanced in time by an explicit four-step Runge–Kutta algorithm which is highly stable and has low storage requirements. Viscous terms are discretized by a standard second-order finite difference scheme and they are included in the residual at the last stage of the Runge–Kutta algorithm. The lower-order integration of the viscous terms is justified by the relatively high Reynolds number of the computed jet. For high Reynolds numbers flows, the time step is imposed by the stability limitation associated with the discretization of Euler fluxes, and is very small compared with the limitation required by the discretization of viscous fluxes. Thus the numerical treatment of the viscous terms is sufficiently accurate. Finally, grid-to-grid oscillations are not resolved by the DRP scheme. To ensure numerical stability, it is necessary to filter them out by using a selective damping of Tam (1995b). The combination of the selective damping with a subgrid scale model based on a turbulent viscosity will have to be studied in further works. However, we should emphasize that their roles are basically different: the selective damping damps only the grid-to-grid oscillations, whereas the subgrid scale model dissipates the turbulent energy through a large range of wave numbers.

2.2. Boundary Conditions

The formulation of boundary conditions is very important in aeroacoustic simulations, because spurious waves reflected when acoustic and aerodynamic fluctuations leave the computational domain may contaminate the physical sound field. Therefore, to predict the sound field directly, acoustic reflections at the boundaries must be minimized.

The two-dimensional formulation developed by Tam and Dong (1996) from the solution of Euler's equations in the acoustic far-field is extended to the three-dimensional case. Their efficiency is mainly due to their multi-dimensional formulation which ensures a continuous treatment along all the boundaries. Two kinds of boundary conditions are considered: a radiation condition at the inflow and the lateral sides of the computational domain, where only acoustic fluctuations are found, and an outflow condition where aerodynamic fluctuations convected by the flow are leaving the computational domain. Further details are provided in Appendix B. Moreover, it is still necessary to implement a sponge zone in the outflow direction to dissipate aerodynamic fluctuations before they reach the boundary, and to filter out possible reflected waves, see Bogey *et al.* (2000). The sponge zone is based on a combination of grid stretching with the introduction of an artificial damping. It is similar to the sponge zone technique proposed by Colonius *et al.* (1993) for noise computation.

2.3. Flow Parameters

The inflow axial velocity of the jet is given by the following hyperbolic-tangent profile:

$$u\left(r\right) = \frac{U_j}{2} + \frac{U_j}{2}\tanh\left(\frac{r_0 - r}{2\delta_\theta}\right),$$

where U_j is the inflow centerline velocity, δ_θ is the initial momentum thickness of the shear layer, and r_0 is the jet radius. The jet Mach number M_j is taken as 0.9, and the fluid surrounding the jet is initially at rest. The jet Reynolds number is $Re_D = U_j \times D/\nu = 65\,000$, and $D = 2r_0 = 3.2 \times 10^{-3}$ m.

The inflow characteristics are important in determining the initial jet structure, typically for one or two diameters just downstream of the nozzle. Experimental ratios between the initial momentum thickness of the shear layer and the initial jet radius, δ_θ/r_0, are very small, less than 10^{-2} as shown in measurements of Zaman (1985). They cannot be reproduced in simulations because of the numerical constraint to discretize the shear layer with enough grid points, and a ratio around 0.1 is usually found in numerical studies. In this study a ratio of 0.05 is chosen, that enables the development of vortical structures in the shear zones, before turbulent mixing occurs on the whole radial section of the jet at the end of the potential core.

To seed the turbulence, the jet is forced using an excitation described in detail in Appendix C. Velocity disturbances are added to the flow in the incoming shear layers. They are solenoidal in order to minimize the production of spurious acoustic waves. They are temporally random and not strongly correlated azimuthally as shown by the correlation function displayed in Appendix C, so that the jet can develop in a natural way, without being influenced by the initial disturbances after one or two diameters downstream from the forcing. Turbulence intensities generated by the forcing are around 4% locally, at the center of the shear layer. This value is in the range of what can be expected for a jet at the present moderate Reynolds number.

2.4. Numerical Specifications

The flow equations are solved on a Cartesian grid of $255 \times 187 \times 127$ points in the three coordinate directions. As represented in Figure 1, meshes are significantly stretched owing to computing requirements. There is high resolution in the jet to calculate turbulent structures very accurately. In this flow region, the turbulent viscosity is of the order of ten times the molecular viscosity. The mesh grid is coarser outside the flow, and is optimized to contain the acoustic field only in the upper radial y direction. In the other transverse directions, the grid does not extend beyond $6r_0$. The sound radiation is therefore investigated in the upper x–y section. It should be noted that a polar grid is more suited to the mean circular geometry since less points are required in far-field, but, for simplicity, Cartesian equations and resolution are chosen, and three-dimensional effects can be similarly investigated in both systems.

Radially, points are clustered in the jet with 26 points in the jet radius. The minimum mesh spacing $\Delta_0 = \delta_\theta/1.6$ is found around $r = r_0$. Outside the jet, mesh spacing increases rapidly, to reach a maximum value of $\Delta y_{\max} = 0.4r_0$. This mesh spacing allows an accurate sound propagation up to a frequency $f_m \simeq c_0/(5\Delta y_{\max})$ corresponding to a Strouhal number $St_m = f_m D/U_j \simeq 1.2$. In the flow direction, mesh spacing is constant up to $x = 20r_0$, with $\Delta x = 3\Delta_0$. Then meshes are stretched for the 40 last points with $\Delta x_{\max} = 0.54r_0$, in order to form a sponge zone. Following the technique used in an earlier study, see Bogey *et al.* (2000), artificial damping is progressively applied in the sponge zone, in the flow region only. Thus, the physical part of the computational domain in the axial direction extends up to $x = 20r_0$ for the flow field, and up to $x = 30r_0$ for the acoustic field.

The time step is $\Delta t = 0.7\Delta_0/c_0$. The simulation runs for 4.5×10^4 iterations, the calculation of statistical means being performed after 5000 iterations. The simulation time is $T_{\text{sim}} \simeq 33 \times L_x/c_0 \simeq 29 \times L_x/U_j$ ($L_x = 30r_0$ is the grid length in the axial direction) which corresponds to a non-dimensional time $T_{\text{sim}}^\star = T_{\text{sim}}U_j/D \simeq 440$. Spectra are computed using the final 3.9×10^4 iterations, on a time period of $T_{\text{sp}}^\star = 1/St_{\min} \simeq 380$. Therefore, the simulation time is likely to be long enough to achieve statistical stationarity. Finally, the computation requires 25 hours on an Nec SX-5, with a CPU time of $0.3\,\mu$s per grid point per iteration.
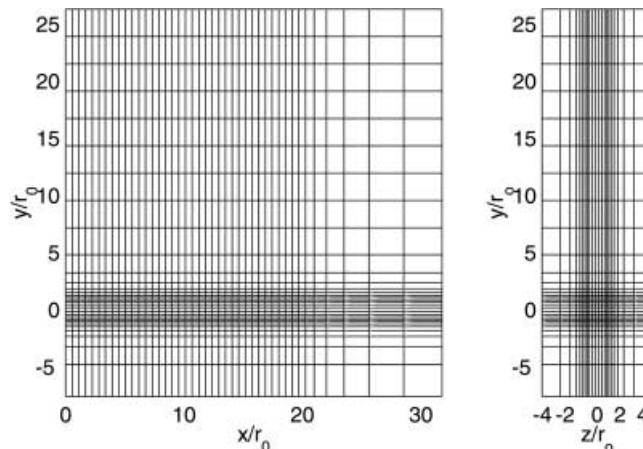

Figure 1. Visualization of the x–y and y–z sections of the Cartesian mesh grid. Only every sixth line in the three coordinate directions is shown.

3. Flow Field

3.1. Flow Development

Figure 2 displays the vorticity fields provided by LES. The axial vorticity field ω_z shows that the initial flow development is likely to be governed by growing instability waves in the shear layer, originating from the forcing disturbances. Large-scale eddies are generated with the rolling-up of the shear layer, for $x \simeq 6r_0$, which initiates the laminar–turbulent transition. Then the mixing zones grow, up to the end of the potential core for about $x = 10r_0$ where they interact and merge. Downstream, a strong typical three-dimensional mixing is found, as illustrated by the transverse vorticity field ω_x, and the flow tends towards developed turbulence.

3.2. Mean Flow Properties

Contours of the mean longitudinal velocity are shown in Figure 3 for velocities varying from $0.05U_j$ up to $0.95U_j$. The potential core (region with uniform velocity U_j) ends around $x \simeq 10r_0$. In the present simulation the inflow excitation is strong enough to have a potential core length corresponding to those obtained for jets with high Reynolds numbers, in which significant turbulent disturbances are found in the initial shear layers. For example, the Mach number 0.9, Reynolds number 10^6 jet of Lau *et al.* (1979) has a potential core length of $10.4r_0$. It should be noted that for very low Reynolds number jets, the core length is generally larger, for
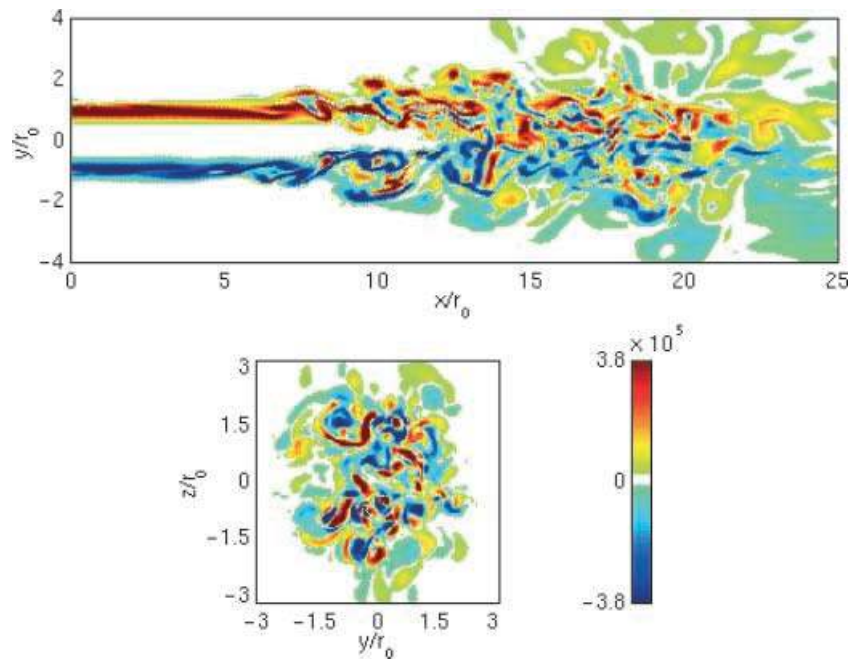

Figure 2. Snapshots of the vorticity field. Upper picture, ω_z in the x–y plane at $z = 0$; bottom picture, ω_x in the y–z plane at $x = 12r_0$. Levels are given in s^{-1}.
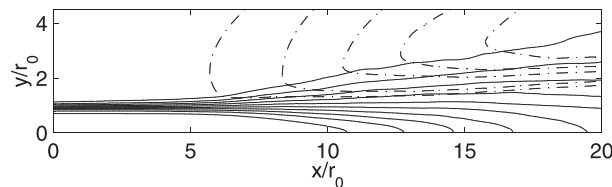

Figure 3. Visualization of mean flow: ——, ten contours of the mean longitudinal velocity defined from $0.05U_j$ to $0.95U_j$; $-\cdot-\cdot$, five streamlines.
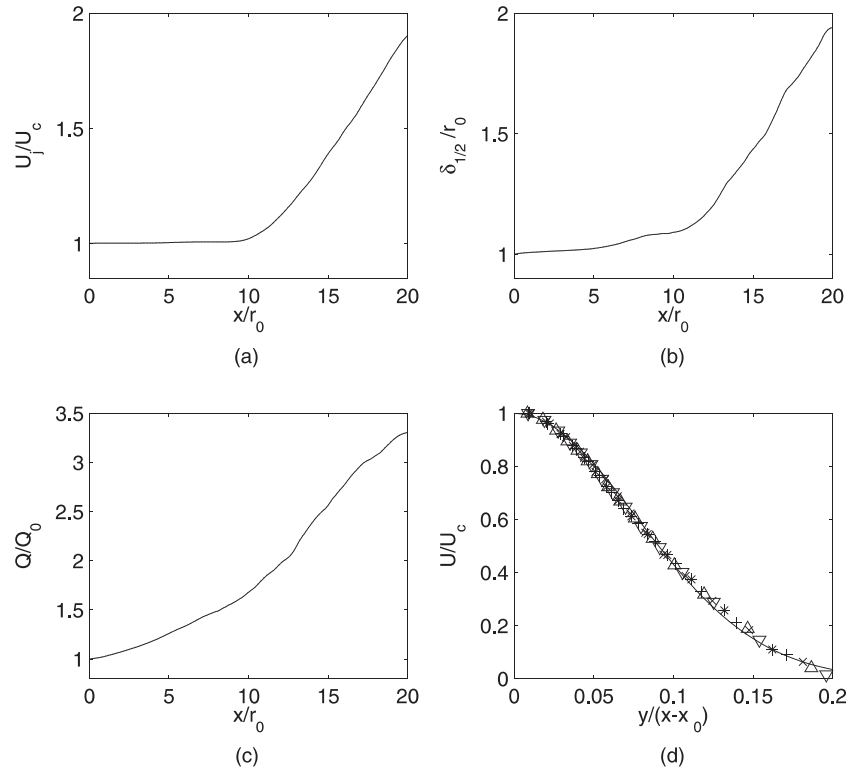
Figure 4. Longitudinal evolution of (a) the inverse of the non-dimensional mean centerline velocity U_j/U_c; (b) the non-dimensional half-width of the jet $\delta_{1/2}/r_0$; and (c) the non-dimensional mean flow rate Q/Q_0. (d) Radial profiles of the mean longitudinal velocity normalized by the local centerline velocity U/U_c: ×, at $x = 15.8r_0$; +, at $x = 16.8r_0$; ∗, at $x = 17.7r_0$; ▽, at $x = 18.6r_0$; △, at $x = 19.6r_0$. ——, approximation with a Gaussian profile.

instance it is $14r_0$ in Stromberg *et al.* (1979) for an $Re_D = 3600$ jet, and this is certainly due to the fact that the incoming flow is laminar.

Some streamlines initiating from points well outside the jet are also plotted in Figure 3. Surrounding fluid, initially at rest, is radially drawn in by the flow at a low speed around $0.02U_j$. This is in accordance with experimental descriptions of the fluid entrainment mechanism. This demonstrates that the boundary conditions implemented in the simulation allow the incoming of fluid into the computational domain to feed the flow. Since fluid entrainment is responsible for the increase of the jet flow rate, its correct modeling is essential to obtain flow characteristics that conform to experiments.

Figure 4 presents the characteristics of the mean flow obtained from the simulation. First, Figure 4(a) displays the longitudinal evolution of the inverse of the mean centerline velocity normalized by the inflow velocity U_j. Its value is 1 in the potential core, and grows linearly afterwards so that we can write $U_c/U_j = B \times D/(x - x_0)$ where $x_0 \simeq 0$ is the virtual origin, and $B \simeq 5.5$ is the decay constant. This value of B is consistent with measurements of Wygnanski and Fiedler (1969), Panchapakesan and Lumley (1993) and Hussein *et al.* (1994), as well as DNS results of Boersma *et al.* (1998), see Table 1. The virtual origin

Table 1. Mean flow parameters obtained from experiments *, DNS ** and the present simulation.

Re_D	B	A	Reference
8.6×10^4	5.4	0.086	Wygnanski and Fiedler (1969)*
1.1×10^4	6.1	0.096	Panchapakesan and Lumley (1993)*
9.5×10^4	5.8	0.094	Hussein *et al.* (1994)*
2.4×10^3	5.9	0.095	Boersma *et al.* (1998)**
6.5×10^4	5.5	0.096	Present simulation

given by the simulation lies in the range of experimental values varying from $x_0 = -5r_0$ for Panchapakesan and Lumley (1993) up to $x_0 = 8r_0$ for Hussein *et al.* (1994). The scattering of these results is due to different Reynolds numbers and initial conditions, and their effect on potential core length.

In the same way, Figure 4(b) presents the longitudinal evolution of the jet half-width normalized with the radius r_0. Its value is nearly 1 up to $x = 6r_0$ where the large vortical structures begin to appear. The jet spreads linearly afterwards in the turbulent region as $\delta_{1/2} = A \times (x - x_0)$, where $A \simeq 0.096$. This is in agreement with the experimental and numerical data of Table 1.

Finally, Figure 4(c) displays the longitudinal evolution of the mean flow rate $Q = \int_S U \, dy \, dz$, where U is the mean axial velocity and S is the transverse section. Its value grows regularly, since the entrainment of the surrounding fluid occurs from the inflow of the computational domain onwards. Its linear growth, deduced from the x^{-1} decay of the centerline velocity and from the linear spreading of the jet, takes place after the potential core, such that $Q/Q_0 = C \times (x - x_0)/D$ where Q_0 is the initial flow rate and $C \simeq 0.32$. Experimental values of this constant are rare in the literature, because they are difficult to measure. Ricou and Spalding (1961) succeeded however in estimating a mass entrainment constant of 0.32, in an air–air jet, corresponding exactly to the simulation result.

The linear longitudinal evolutions of parameters $1/U_c$, $\delta_{1/2}$ and Q suggest that the self-similarity region of the jet is reached in the simulation. To confirm this, radial profiles of the mean axial velocity normalized by the centerline velocity U_c are plotted in Figure 4(d) as a function of the non-dimensional coordinate $y/(x - x_0)$, for five locations between $x = 15r_0$ and $x = 20r_0$. The constant A is then given by the half-width of the profiles and these curves are superimposed. It is interesting to notice that the mean radial profile is well approximated by the Gaussian function $U/U_c = \exp\left(-K_u \left(y/(x - x_0)\right)^2\right)$ found experimentally, where the constant K_u is related to the constant A by the relation $K_u = \ln 2/A^2$.

3.3. Turbulence Intensities

Turbulence intensities provided by LES are now investigated. The longitudinal, radial and azimuthal intensities, σ_{uu}, σ_{vv} and σ_{ww}, are calculated in the x–y plane at $z = 0$, using fluctuating velocities u', v' and w'. They are given by $\sigma_{uu} = \sqrt{\langle u'^2 \rangle}/U_c$, $\sigma_{vv} = \sqrt{\langle v'^2 \rangle}/U_c$ and $\sigma_{ww} = \sqrt{\langle w'^2 \rangle}/U_c$, where $\langle \cdot \rangle$ denotes the time averaging. The Reynolds stress intensity σ_{uv} is also defined by $\sigma_{uv} = \sqrt{|\langle u'v' \rangle|}/U_c$. These intensities are normalized with the local centerline longitudinal velocity, according to usual representation.

Longitudinal profiles of the turbulence intensity σ_{uu} in the shear layer and in the jet centerline are displayed in Figure 5. To check the transition in the shear layers in Figure 5(a), turbulence intensity is presented in a logarithmic scale for $0 < x/r_0 < 10$ where $\sigma_{uu} \simeq \sqrt{\langle u'^2 \rangle}/U_j$. From an initial value of 4% generated by the forcing, it then increases linearly until $x \simeq 8r_0$. This shows the exponential development of the instabilities in the shear layers with a growth rate $-k_i r_0 = 0.205$. This rate is lower than rates usually predicted by linear instability analysis for the most unstable frequency of the initial profile. Two discrepancies with a simple linear analysis exist. First the amplitudes are strong enough for important nonlinearities to occur. Second,
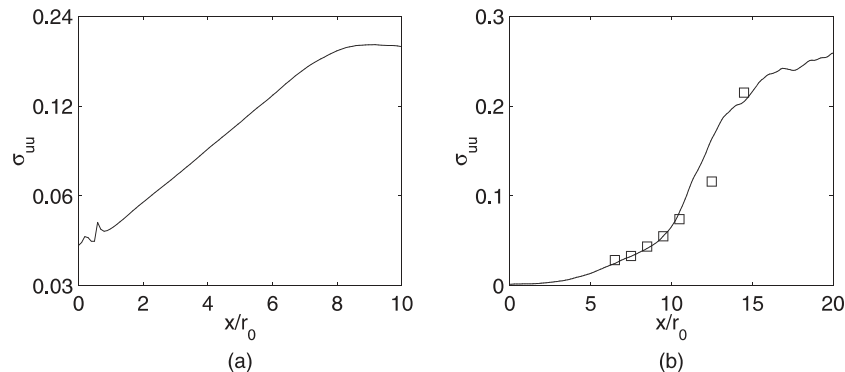

Figure 5. Profiles of the longitudinal turbulence intensity σ_{uu}: (a) in the shear layer at $z = 0$ and $y = r_0$, in a logarithmic scale; (b) in the jet centerline, in a linear scale. □ measurements of Lau *et al.* (1979) shifted by $-1.5r_0$ in the axial direction.

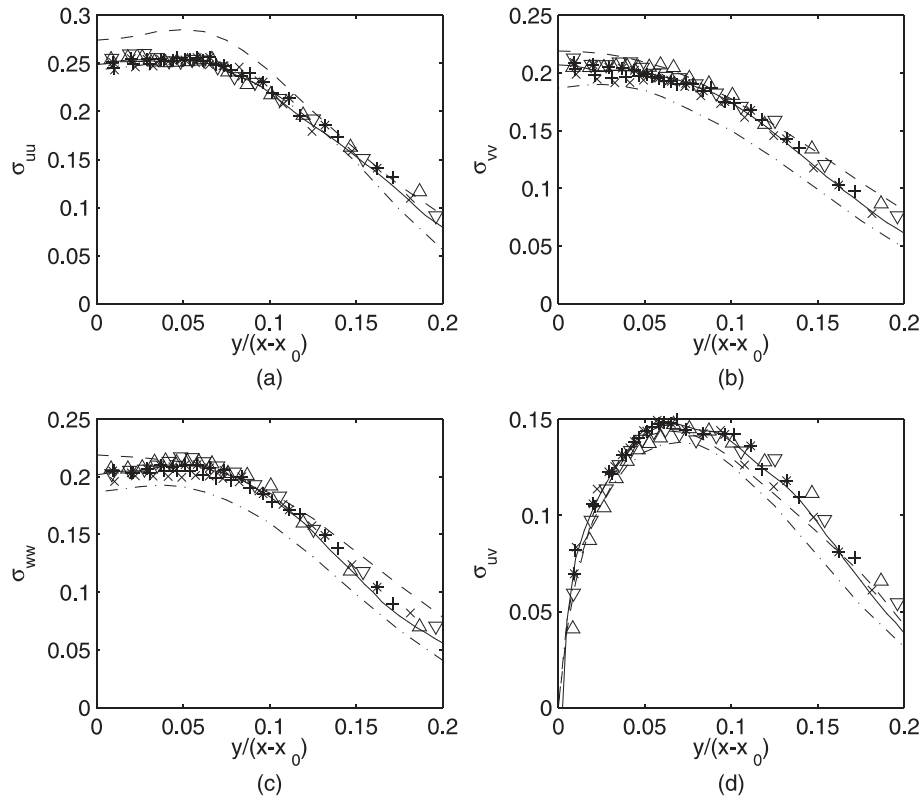**Figure 6.** Radial profiles of the turbulence intensities: (a), σ_{uu}, (b), σ_{vv}, (c), σ_{ww}, (d), σ_{uv}. $\times$, at $x = 15.8r_0$; $+$, at $x = 16.8r_0$; $*$, at $x = 17.7r_0$; $\bigtriangledown$, at $x = 18.6r_0$; $\triangle$, at $x = 19.6r_0$. ——, mean profiles calculated from $x = 15r_0$ to $x = 20r_0$; $-\cdot-\cdot$, experimental profiles obtained by Panchapakesan and Lumley (1993); $-\,-\,-$, experimental profiles obtained by Hussein *et al.* (1994).

the spectra are broadband, as shown in the next subsection, and the growth rate of a single frequency cannot be compared with the total growth rate.

The centerline profile presented in Figure 5(b) shows that the intensity is negligible at the inflow owing to the excitation being applied only in the shear layers. It increases significantly only after the end of the potential core around $x \simeq 10r_0$, to reach a value of the order of 0.25 for $x > 15r_0$. This result shows that the averaging time $T_{\mathrm{av}} \simeq 20 \times L_x/U_j$ is long enough to make the mean turbulence intensities converge to steady values. It supports the assumption that turbulence is fully developed and that jet self-similarity is verified for $x > 15r_0$. The transition from laminar to turbulent flow between $x = 5r_0$ and $x = 15r_0$ is also consistent with the experiment of Lau *et al.* (1979). Turbulence intensities provided by Lau *et al.*, shifted by $-1.5r_0$ in the axial direction to account for the different initial conditions, coincide well with the simulation curve.

Radial profiles of the turbulence intensities are shown in Figure 6 for five locations between $x = 15r_0$ and $x = 20r_0$, as a function of the non-dimensional coordinate $y/(x - x_0)$. Profiles are well superimposed, which is in agreement with the self-similarity of fully turbulent jets. The mean profiles calculated between $x = 15r_0$ and $x = 20r_0$ are also plotted as solid lines. They are very close to measurements, and fall between two experimental profiles provided by Panchapakesan and Lumley (1993) and Hussein *et al.* (1994). Thus, turbulence levels supplied by LES agree very well with experimental data.

3.4. Turbulence Integral Length Scales

Experiments conducted by Davies *et al.* (1963) and Wygnanski *et al.* (1969) have shown the evolution of turbulence length scales in the three following jet zones: the shear layers, the zone just after the potential core and the self-similarity zone. In the shear layers, the length scales initially increase rapidly and linearly with the axial distance. Further downstream, after the disappearance of the potential core, the turbulent structures
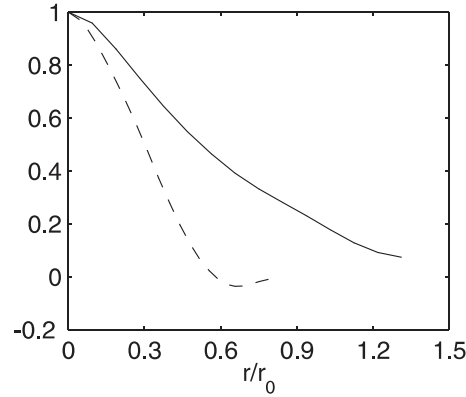
Figure 7. Evolution of correlation functions at the point defined by $x = 16.8r_0$ and $y = z = 0$: ——, $R_{11}^{(1)}(r)$; − − −, $R_{11}^{(2)}(r)$.

Table 2. Integral length scales found on the jet axis.

$L_{11}^{(1)}/x$	$L_{11}^{(2)}/x$	$L_{11}^{(1)}/L_{11}^{(2)}$	Reference
0.0385	0.0157	2.43	Wygnanski and Fiedler (1969)
0.037	0.017	2.14	Present simulation

are mixed over the whole jet section and their length scales tend to decrease. Finally, in the self-similarity region with developed turbulence, length scales increase again linearly with the axial distance, but more slowly than in the shear layers.

Integral length scales are now estimated in the jet self-similarity zone, at $x = 16.8r_0$ on the jet axis. With this aim in view, Figure 7 presents the evolution of the correlation functions of the axial fluctuating velocity, $R_{11}^{(1)}(r)$ and $R_{11}^{(2)}(r)$, computed at the point (x, y, z) by

$$R_{11}^{(1)}(r) = \frac{\langle u'(x,y,z) \times u'(x+r,y,z) \rangle}{\langle u'^2(x,y,z) \rangle^{1/2} \times \langle u'^2(x+r,y,z) \rangle^{1/2}},$$

$$R_{11}^{(2)}(r) = \frac{\langle u'(x,y,z) \times u'(x,y+r,z) \rangle}{\langle u'^2(x,y,z) \rangle^{1/2} \times \langle u'^2(x,y+r,z) \rangle^{1/2}}.$$

The behavior of these two functions agrees well with experimental results, reported for instance by Wygnanski and Fiedler (1969). In particular, the $R_{11}^{(2)}(r)$ function takes negative values for large distances.

The integral scales defined by $L_{11}^{(1)} = \int_0^\infty R_{11}^{(1)}(r)\,\mathrm{d}r$ and $L_{22}^{(1)} = \int_0^\infty R_{22}^{(1)}(r)\,\mathrm{d}r$ are respectively $L_{11}^{(1)} = 0.62r_0$ and $L_{11}^{(2)} = 0.29r_0$. They are well discretized since $\Delta x \simeq 0.05r_0$ and $\Delta y \simeq 0.03r_0$ at the study point. Moreover, because of the linear increase of integral scales with x, the ratios $L_{11}^{(1)}/x$ and $L_{11}^{(2)}/x$ are constant in a turbulent jet. Thus the ratios evaluated in the simulation can be compared with ratios given by Wygnanski and Fiedler (1969) on the axis of a jet in its self-similarity zone and presented in Table 2. Both are in very good agreement. The ratio $L_{11}^{(1)}/L_{11}^{(2)}$ is also close to the measurement, and it is slightly higher than the value of 2 found for a homogeneous isotropic turbulence. In this way, the turbulent field provided by the simulation is validated both in terms of intensity and length scales, or respectively, one and two point correlations.

3.5. Spectra of Velocity Fluctuations

The time histories of fluctuating radial velocity have been recorded at $y = r_0$ and $z = 0$ in the shear layers for four distances from the inflow, during the final 39 000 iterations. Spectral power densities are obtained from these signals. We can expect to find the fundamental frequency f_0 of the initial hyperbolic-tangent profile, at least for the first study point. It is predicted by the linear theory of instabilities developed by Michalke (1964), and corresponds to a Strouhal number of $St = 0.68$. Spectra are calculated from a time sample T_{sp} such as $T_{sp} \times f_0 \simeq 260$, and have therefore converged.
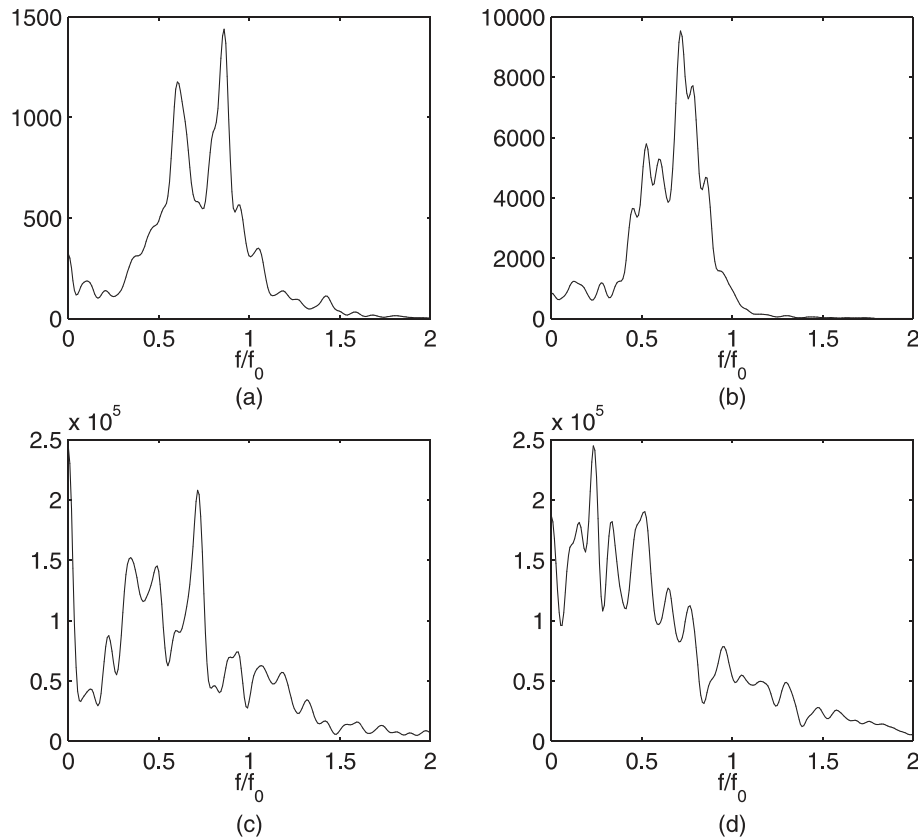
Figure 8. Power spectral density of the fluctuating radial velocity at four locations in the shear layer, at $y = r_0$ and $z = 0$; (a) $x = 2.4r_0$; (b) $x = 4.4r_0$; (c) $x = 8.5r_0$; (d) $x = 12.6r_0$. f_0 is the fundamental frequency of the hyperbolic-tangent profile provided by the linear theory of instabilities. (f_0 corresponds to a Strouhal number of $St = 0.68$.)

The four spectra are presented in Figure 8. We can notice the difference of magnitude in the first three spectra, with around one order between two successive ones. This shows the rapid growth of instability waves in the shear layer in the early stage of jet development. The spectra also all appear to be broadband, which suggests nonlinear broadening.

In Figure 8(a), at $x = 2.4r_0$ near the inflow, two peaks are clearly visible in the spectrum. Since the inflow forcing is random, the velocity profile has selected particular frequencies. The most amplified frequency is close to but slightly lower than the fundamental frequency f_0. As shown by the growth of turbulence intensities in the shear layer, the linear instability basically derived for a parallel shear flow cannot fully describe the initial development. The second frequency peak is two-thirds of the frequency of the primary instability. Following the discussion conducted by Stromberg *et al.* (1980), the instability mode is likely to be helical rather than axisymmetric.

The three other spectra given in Figure 8 are comparable with spectra given by Stromberg *et al.* (1980) at $x = 10r_0$, $x = 14r_0$ and $x = 16r_0$ from the nozzle exit, for a Mach 0.9, $Re_D = 3600$ jet. This demonstrates that the transition in the shear layers is consistent with experimental observations in terms of spectral contents. Moreover, the apparent shift of the order of $5r_0$ between computation and experiment, already observed for the potential core length, is almost certainly due to the different inflow conditions. In Figure 8(b) at $x = 4.4r_0$, a narrow spectral band dominates the spectrum with a maximum for $St = 0.48$. An $St = 0.44$ was found experimentally in Stromberg *et al.* (1980). In Figure 8(c), at $x = 8.5r_0$, the spectrum becomes richer in high-order subharmonic frequencies related to large structures, while high frequencies associated with small-scale turbulence appear. Finally, a spectrum dominated by frequencies between $St = 0.1$ and $St = 0.6$ is obtained at $x = 12.6r_0$ in Figure 8(d). We can also note that the flow downstream from the potential core is transitional, but not fully turbulent.

3.6. Turbulent Spectrum

The spectrum of the turbulent kinetic energy $\langle u_1'^2 + u_2'^2 + u_3'^2 \rangle/2$ is calculated in the fully turbulent jet at the point $y = r_0$, $z = 0$ and $x = 16.8r_0$, from the same time T_{sp} as in the previous subsection, and is plotted in Figure 9. The Taylor hypothesis of frozen turbulence is used to estimate $E_k^{(1)}(k_1)$ from the temporal spectrum $E_f(f)$. Assuming that wave number and frequency are related by $k_1 = 2\pi f/U$ with U the mean axial velocity, we can then write

$$\frac{1}{2}\langle u_1'^2 + u_2'^2 + u_3'^2 \rangle = \int\limits_0^\infty E_f(f)\,\mathrm{d}f = \int\limits_0^\infty E_f(f)\frac{U}{2\pi}\,\mathrm{d}k_1 = \int\limits_0^\infty E_k^{(1)}(k_1)\,\mathrm{d}k_1\ .$$

Using jet parameters in the relations of isotropic turbulence, the Kolmogorov and Taylor scales are calculated to be $\eta = \left(L_{11}^{(1)}\right)^{1/4}\left(\nu/u_1'\right)^{3/4} = 2 \times 10^{-6}$ m and $\lambda_g = \left(15L_{11}^{(1)}\nu/u_1'\right)^{1/2} = 6.5 \times 10^{-5}$ m, and the longitudinal integral length scale is $L_{11}^{(1)} = 8.9 \times 10^{-4}$ m. The large difference between λ_g and η indicates that an inertial zone is likely to be found in the spectrum. This is the case in the computed results as shown by the typical $k_1^{-5/3}$ slope in Figure 9. The Kolmogorov wave number is equal to $k_\eta = 1/\eta = 5 \times 10^5$ m^{-1}. It is higher than the grid cut-off wave number also represented in Figure 9 and given by $k_c = 2\pi/(5\Delta_c)$, where Δ_c is the local mean mesh spacing, corresponding to the highest wave number well resolved by the numerical algorithm with six points per wavelength. This cut-off wave number is located in the inertial zone, therefore supporting an assumption of the subgrid scale model, and the spectrum decreases rapidly afterwards as expected.

A cut-off Strouhal number $St_c = f_c D/U_j$ where $f_c = k_c U/(2\pi)$ can be associated with the grid cut-off wave number, for example $St_c \simeq 2.5$ in Figure 9. The local grid cut-off Strouhal number is represented in Figure 10 for the whole jet. It is between 2 and 5 in the jet, and more especially between 4 and 5 at the end of the potential core in the zone where the predominant sound sources are located. Since the preferred range of jet radiation has been experimentally found for $0.1 < St < 1$ by Mollo-Christensen et al. (1964), Lush (1971), Stromberg et al. (1979) and Juvé et al. (1980), most of the significant sound sources are resolved by the simulation.
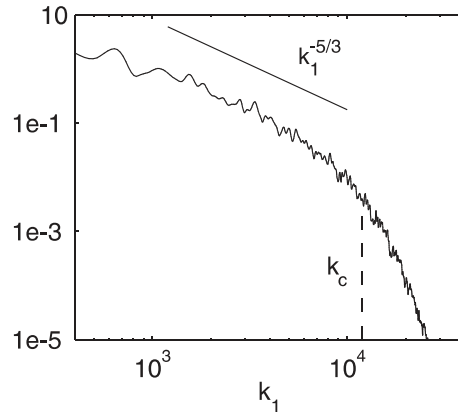

Figure 9. Turbulent kinetic energy spectrum $E_k^{(1)}(k_1)$ at $x = 16.8r_0$, $y = r_0$ and $z = 0$.
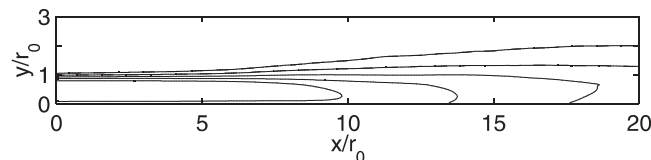

Figure 10. Visualization of the aerodynamic grid cut-off Strouhal number St_c. Five contours defined from 5 in the jet to 1 outside with a decrement of 1.

4. Acoustic Field

4.1. Instantaneous Dilatation Field

Figure 11 displays, in the plane $z = 0$, the instantaneous dilatation field $\Theta = \nabla \cdot \mathbf{u}$ in the acoustic region and the vorticity field ω_{xy} in the flow region, obtained directly from the simulation. Dilatation accounts for compressible fluctuations only, and is linked to the acoustic pressure outside the flow by

$$\Theta = \nabla \cdot \mathbf{u} = -\frac{1}{\varrho_0 c_0^2} \frac{\partial p}{\partial t} . \tag{1}$$

Dilatation is thus proportional to the time derivative of the pressure outside the jet. Its use allows the elimination of any slow drift in the mean pressure field and the filtering out of very low frequency waves.

Acoustic wave fronts generated by the turbulent jet are clearly visible in Figure 11. Any sound waves that might be generated by the inflow excitation or by the exit of turbulent structures at the outflow are detected in the dilatation field. Waves fronts originate from the region where the mixing layers merge around $x = 11r_0$. Predominant sound sources are therefore indicated in the region slightly after the end of the potential core. This agrees both with the results of the recent DNS performed by Freund (2001) and with the measurements of Chu and Kaplan (1976) and Juvé *et al.* (1980) using various sound source localization techniques. The sound field directivity is also much more pronounced in the downstream direction, in accordance with experiments.

4.2. Acoustic Fluctuations

To investigate the sound field properties, pressure and dilatation are recorded in the acoustic field during the final 39 000 iterations, at different locations along the boundaries of the computational domain. As an illustration, Figure 12 shows the simultaneous time traces of the fluctuating pressure and dilatation obtained at $x = 10r_0$, $y = 24r_0$ and $z = 0$. The pressure fluctuation appears to be composed of two components: waves
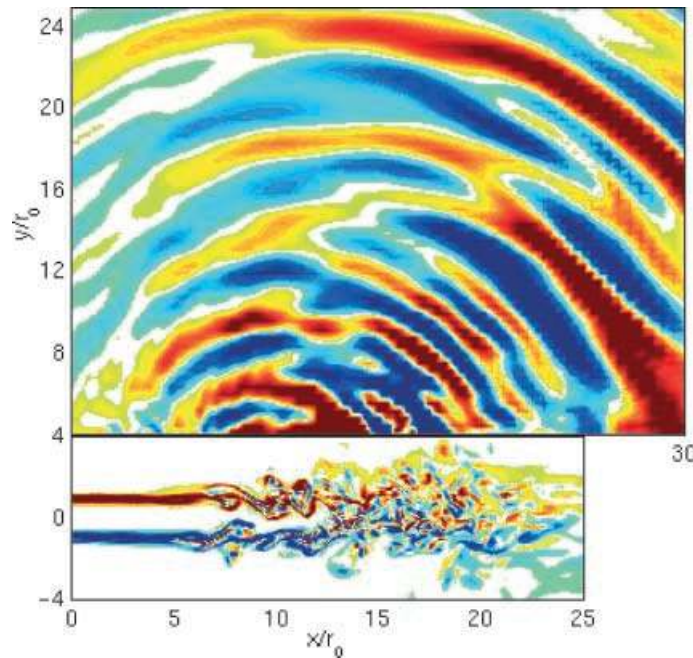

Figure 11. Snapshot of the dilatation field $\Theta = \nabla \cdot \mathbf{u}$ in the acoustic region, and of the vorticity field ω_z in the aerodynamic region, in the x–y plane at $z = 0$. The dilatation color scale is defined for levels from -90 to $90\,\mathrm{s}^{-1}$, the vorticity scale is the same as in Figure 2.
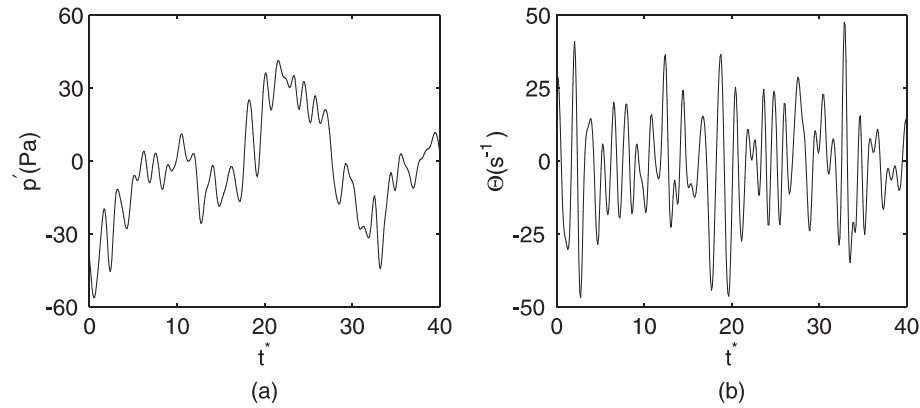
Figure 12. Time evolution of (a) the pressure and (b) the dilatation; recorded at $x = 10r_0$, $y = 24r_0$ and $z = 0$, as a function of non-dimensional time $t^* = tU_j/D = 1/St$.

characterized by Strouhal numbers $St \simeq 0.3$, and low frequency oscillations with $St \simeq 0.06$. The low frequency waves can be considered as spurious sound waves, and they are probably due to reflections at the outflow boundary, because the sponge zone is built up over only 40 points owing to numerical constraints. The low frequency waves resolved by the maximum grid spacing in the downstream direction are not very dissipated by the artificial damping. In an ealier simulation of a two-dimensional mixing layer in Bogey (2000), a 100 point sponge zone was used and the spurious waves were then significantly reduced.

The spectrum of the fluctuating pressure is calculated from all the recordings so that the sampling period is $T_{sp}^\star = T_{sp}U_j/D = 1/St_{min} \simeq 380$. Pressure and dilatation signals can be used indifferently. When working with the dilatation signal, the pressure spectrum is deduced from the dilatation spectrum thanks to the Fourier transform of relation (1) giving in modulus

$$p(f) = \frac{\varrho_0 c_0^2}{2\pi f} \, \Theta(f) \, . \tag{2}$$

The two computed spectra are displayed in Figure 13(a), and they are exactly superimposed except for very low frequencies where relation (2) diverges. The use of pressure or of dilatation is therefore equivalent to describe the acoustic field.

Figure 13(b) presents the pressure spectrum in a logarithmic scale. For $St \leq 0.1$, the spectrum corresponds to the spurious waves, with a peak of $St \simeq 0.06$ in agreement with previous observations. For $St > 0.1$, the spectrum can be associated with physical waves, and shows the typical shape of an acoustic spectrum for a moderate Reynolds number jet, at an observation angle close to 90°. The radiation range $0.1 < St < 0.6$
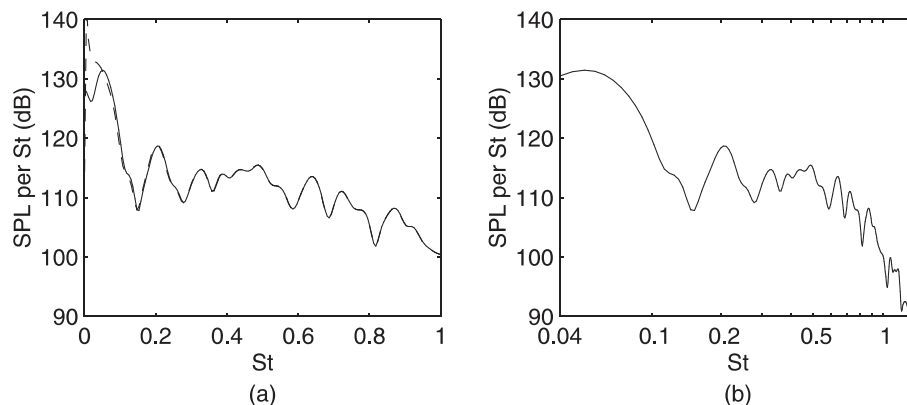
Figure 13. Sound pressure spectra obtained at the point defined in Figure 12, as a function of Strouhal number $St = fD/U_j$, from the pressure (——) and the dilatation (− − −). (a) Linear scale and (b) logarithmic scale.

corresponds to the preferred range of radiation found experimentally, as for instance in Juvé *et al.* (1980). The rapid decrease of the spectrum around $St \simeq 1$ can certainly be attributed to the maximum grid frequency in the acoustic field.

4.3. Sound Pressure Spectra

Figures 14 shows the sound pressure spectra obtained for angles of 30° and 90° from the downstream jet axis, respectively, at a constant distance of $60r_0$ from the jet inflow. Only Strouhal numbers greater than 0.15 are considered in accordance with the observations of Section 4.2. The radiation distance of $60r_0$ has been chosen to make comparisons possible with experimental directivities, for which origins are taken at the jet nozzle exit. Calculation of the spectra is moreover simply done by using the r^{-1} decay of acoustic waves from the source region located at $x = 11r_0$ to the far field. Remember that the sampling time is $T^{\star}_{sp} = 1/St_{min} \simeq 380$, and thus contains 380 and 76 periods, respectively, for $St = 1$ and $St = 0.2$ frequencies. This time is divided into 12 overlapping sections. Therefore, we can expect the spectra to be fairly converged. For further studies, to accelerate the statistical convergence and to obtain experiment-like spectra, it would be helpful to average in the azimuthal direction.

Figure 14 shows that sound levels for $\theta = 30°$ are more than 10 dB higher than for $\theta = 90°$. Spectra are not fundamentally different, and both reach a peak for a Strouhal number abound $St \simeq 0.2$. This frequency peak is in accordance with the experimental observations of Stromberg *et al.* (1980) on an $Re_D = 3.6 \times 10^3$ jet, and by Long and Arndt (1984) on an $Re_D = 8.5 \times 10^4$ jet. The evolution of the spectrum shape as a function of the observation angle is also in good agreement with the results of Long and Arndt (1984). Thus, as expected, the spectra of the present moderate Reynolds number jet are comparable with those measured for jets at low Reynolds numbers. In particular, a broadband high frequency spectrum is not found for $\theta = 90°$ as, for instance, in the jets of Lush (1971) at higher Reynolds numbers.

4.4. Acoustic Directivity

The pressure spectra are now integrated to provide the sound directivity. The portion of the physical sound spectrum for $St < 0.15$ is neglected. To support this, the spectra of Juvé *et al.* (1980), measured for $M = 0.4$ and $Re_D = 1.8 \times 10^5$ jet, have been integrated with and without the $St < 0.15$ band. Level differences are 0.4 dB for an angle of $\theta = 90°$ and 0.6 dB for $\theta = 30°$. The pressure spectra are also limited at high frequencies by the maximum Strouhal number $St_m \simeq 1.2$ resolved by the grid in the acoustic field. The same spectra as above have been integrated with and without the $St > 1.2$ band, and level differences are 0.6 dB for $\theta = 90°$ and 0.3 dB for $\theta = 30°$. In all cases with partial integration, underestimation of pressure levels is of the order of only 1 dB.

The sound pressure levels are shown in Figure 15 with experimental data for jets with similar Mach numbers but various Reynolds numbers as reported in Table 3. The agreement between calculated and measured
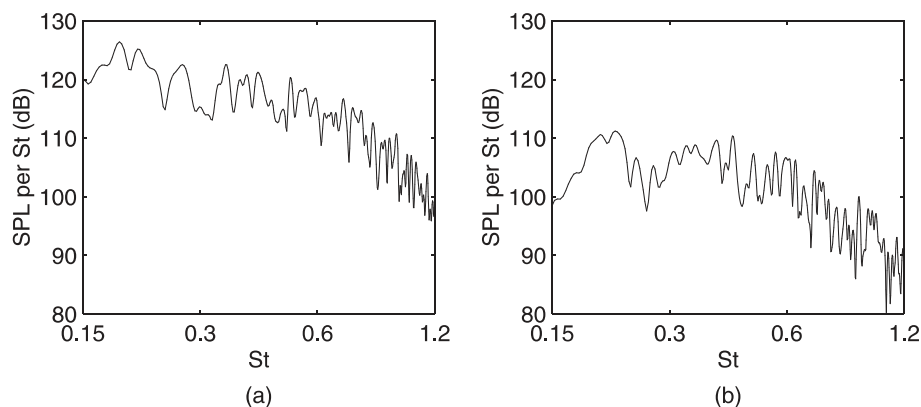
Figure 14. Sound pressure spectra as a function of Strouhal number $St = fD/U_j$, at $60r_0$ from the inflow, for an angle of (a) $\theta = 30°$ and (b) $\theta = 90°$.
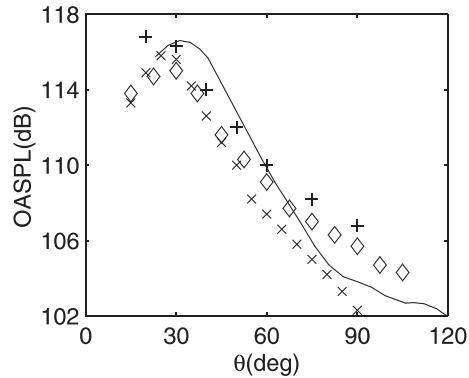
Figure 15. Overall sound pressure level as a function of angle θ measured from the jet axis, at $60r_0$ from the jet nozzle. Experimental data by: $+$, Mollo-Christensen *et al.* (1964); $\diamond$, Lush (1971); $\times$, Stromberg *et al.* (1980).

Table 3. Some jet sound field experiments with Mach numbers similar to that of the present simulation.

M	Re_D	Reference
0.9	5.4×10^5	Mollo-Christensen *et al.* (1964)
0.88	5×10^5	Lush (1971)
0.9	3600	Stromberg *et al.* (1979)
0.9	6.5×10^4	Present simulation

sound levels is very good for all observation angles. As expected, the acoustic level reaches a peak around an angle of $\theta = 30°$. At larger observation angles, the levels decrease rapidly, and fall between the experimental data.

The sound directivity results from a complex combination of convective amplification and mean flow–acoustic interaction effects, which is not discussed here but can be found in Lilley (1994). However, some observations can be made from the different experimental results. For $\theta > 90°$, levels are relatively scattered, with for example 4 dB between levels provided by Lush (1971) and by Stromberg *et al.* (1979). This behavior is associated with a Reynolds number effect, and suggests that small-scale turbulence is responsible for the main part of the noise for large angles. In the downstream direction, however, there are similarities between the acoustic radiations of jets with very different Reynolds numbers varying from 3600 up to 5.4×10^5. This suggests that the noise generation in the jet axis direction may be relatively independent of the Reynolds number.

Sound sources are likely to be well described in the simulation since the sound field is in good agreement with measurements at moderate Reynolds numbers in terms of directivity, spectra and levels. Then we can now investigate in detail the links existing between the dynamics of turbulent structures and acoustic emission.

5. Investigation of Noise Sources

5.1. Introduction

Although the role of large-scale structures in subsonic jet noise is recognized by many authors, the generation mechanism is not clearly identified. Pairings of coherent structures were proposed by Laufer *et al.* (1974) to be the predominant noise source. They can radiate intensely, in particular when they are controlled by an appropriate jet excitation as in the experiments of Kibens (1980), but they may not represent the main contribution of sound sources. Among the facts supporting this, we can mention that for most jets, shear layers being initially turbulent, very few pairings occur. The pairings of purely axisymmetric coherent structures generate a very typical directivity shown experimentally by Bridges and Hussain (1992) which is quite different from the classical jet noise directivity. To deal with the problem of noise generation by pairings,

it is necessary to consider pairings in a more general way as the interactions between two distinct vortical regions, and to note that sound generation proceeds not only from the merger of turbulent structures but also from their mutual interactions via induced velocities. Hussain (1986) for instance has suggested that it is the breakdown process of the toroidal structures into substructures near the end of the potential core that produces most noise. However, it is still difficult to look into the proposed theories, because of the flow complexity.

A classical attempt to identify noise sources consists in performing causality correlations, as in Schaffar (1979) or in Juvé *et al.* (1980) for instance. Nevertheless, for a temporally random turbulent flow, it is very difficult to find convincing correlations between the acoustic field and the flow field, and only the case of excited flows provides a direct connection between the coherent structures within the jet shear layers and the observed noise. Although these difficulties tackled in experiments remain in numerical investigations, simulations providing the space–time evolution of both flow field and acoustic radiation constitute a new opportunity to understand the link between flow and acoustics.

5.2. Connection between Flow Field and Acoustic Field

In the present simulation, animations of visualizations of both the flow and the acoustic radiation suggest that the noise comes principally from the region where the shear layers merge, at the end of the potential core. To establish this, the pressure and the norm ω of the vorticity vector in the jet have been recorded every 45 iterations during 4050 time steps. The non-dimensional recording time is $t^* = tU_j/D = 39.6$ with $\Delta t^* = 0.44$. The pressure is filtered out for $St < 0.12$ so that only the fluctuating pressure p' corresponding to physical waves is used.

The pressure obtained in the plane $z = 0$, at points $(x = 24.8r_0, y = 8r_0)$ and $(x = 16r_0, y = 8r_0)$, is displayed in Figure 16. These points are at distances of $16r_0$ and $9.4r_0$, respectively, from the apparent location of sound sources at $(x = 11r_0, y = z = 0)$, at angles of about $\hat{\theta} = 30°$ and $\hat{\theta} = 60°$ with respect to the downstream direction ($\hat{\theta}$ denotes an angle taken from the source location). The pressure signal for $\hat{\theta} = 30°$ in Figure 16(a) clearly has a low frequency periodic behavior with a predominant period corresponding to a Strouhal number of $St \simeq 0.2$. This value is in agreement with the peak measured in the sound spectra reported in Figure 14. The pressure signal for $\hat{\theta} = 60°$ in Figure 16(b) contains more high frequency waves than for $\hat{\theta} = 30°$, but still shows a fundamental oscillation at $St \simeq 0.2$. These observations indicate that a single sound source is responsible for a very large part of the noise in the downstream direction, but that other additional sources radiate for wider angles.

To detect the sound sources, we consider the wave front with the highest amplitude in each of the two pressure signals. For $\hat{\theta} = 30°$, it is obtained for $t^* = 13.2$ and it is part of the $St \simeq 0.2$ oscillation. This front is presented in Figure 17(a) and has a directivity well pronounced in the downstream direction with a maximum around 30°, consistent with the typical jet noise pattern. For $\hat{\theta} = 60°$ the largest amplitude is detected for $t^* = 6.9$. It cannot be related to another wave front and may correspond to an isolated flow event. As shown
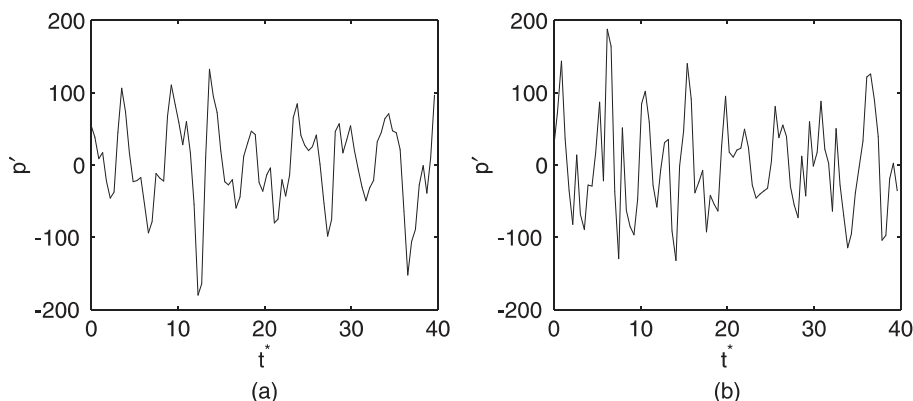

Figure 16. Time evolution of the fluctuating pressure in Pa, as a function of the non-dimensional time $t^* = tU_j/D = 1/St$ for (a) $x = 24.8r_0$, $y = 8r_0$ and $z = 0$, for $\hat{\theta} = 30°$ and (b) $x = 16r_0$, $y = 8r_0$ and $z = 0$, for $\hat{\theta} = 60°$.
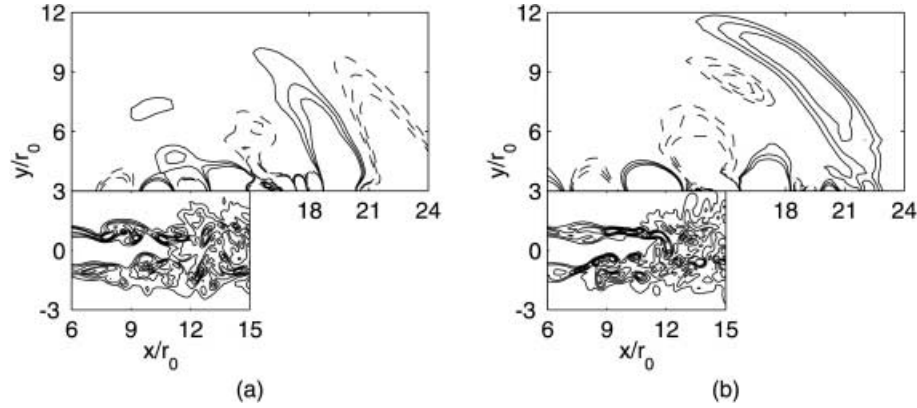
Figure 17. Snapshot of the fluctuating pressure p' in the acoustic field and of the vorticity ω in the flow field in the plane $z = 0$ at times (a) $t^* = 11$ and (b) $t^* = 7.5$. Vorticity contours: $[0.6, 1.2, 1.8, 2.4, 3] \times 10^5$ m s^{-2}. Pressure contours: ——, $[70, 100, 130]$ Pa; $---$, $[-130, -100, -70]$ Pa.

in Figure 17(b), this radiation is important for angles between 30° and 70°, unlike the integrated jet noise directivity.

To connect the acoustic radiation with flow events, the non-dimensional time delay $\Delta t_r^* = \Delta t_r U_j / D$ between the emission and the arrival in the acoustic field of the sound waves, is evaluated by assuming a source location close to $(x = 11r_0, y = z = 0)$ and a wave propagation at the mean sound speed c_0. We find $\Delta t_r^* = 7.1$ and $\Delta t_r^* = 4.2$, respectively, for the two points at $\hat{\theta} = 30°$ and $\hat{\theta} = 60°$. The flow is now investigated in the plane $z = 0$. It is important to note that events involved in noise generation could have taken place out of this two-dimensional slice, but it is reasonable to think that the events at the origin of the two high amplitude sound waves shown above can be detected in this slice.

For the wave front obtained at $\hat{\theta} = 30°$, the emission time is approximately $t^* = 6.1$, but it is certainly a little later because the sound propagation takes place largely in the flow region. The vorticity field is then shown at times $t^* = 6.2$ and $t^* = 7.5$ in Figure 18. The shear layers of the jet are distinguishable up to $x = 15r_0$ in Figure 18(a), but only up to $x = 11r_0$ in Figure 18(b). Turbulent structures initially in the shear layers have penetrated the jet core near $x = 11r_0$, and they are suddenly accelerated by the higher flow velocity. At the same time, we can observe that the shear layer is locally stretched. This breakdown of the shear layers in the jet core seems to be the source of the noise generated in the downstream direction.

For the wave front obtained at $\hat{\theta} = 60°$, the generation occurs for $t^* = 2.7$. Vorticity is thus shown at times $t^* = 2.2$ and $t^* = 3.5$ in Figure 19. A large coherent structure isolated from other ones, located by $x \simeq 11r_0$ and $y \simeq r_0$, is observed in the upper shear layer in Figure 19(a). It interacts with others to merge with the vortical field located downstream as shown in Figure 19(b). This kind of vortex pairing could be responsible for the strong radiation observed in the pressure signal.

5.3. Correlation between the Predominant Radiation and the Breakdown of Shear Layers

We now attempt to show that a correlation exists between the sound radiation predominant in the downstream direction, and the breakdown of shear layers in the jet near the end of the potential core. As it is difficult to interpret the signals of velocity or vorticity in the jet directly, because of their random behavior, a new simple indicator of the presence of vortical structures in the vicinity of the jet axis is introduced. It is the distance $\delta_{sl}(x)$ between the shear layers in the plane $z = 0$, and this transverse length is computed using a threshold of magnitude vorticity $\omega \leq 5 \times 10^4$ m s^{-2}. This value is chosen arbitrarily, but the comparison with the scales used in Figure 18 suggests that the vorticity can be considered as negligible below this level.

A space–time representation of δ_{sl} downstream of the potential core is provided in Figure 20. The black regions are determined by the criterion $\delta_{sl} \leq 0.05r_0$, and they point out that turbulence is significantly present in the jet core. They begin around $x = 12r_0$, but more interestingly, they are clearly distinct and distributed regularly in time. This shows that the shear layers break down in the jet intermittently, and even quasi-periodically, in the vicinity of $x = 11r_0$ just after the potential core. In the period between two breakdowns, the shear layers grow continuously as in Figure 18(b) and no turbulence is found on the jet axis.
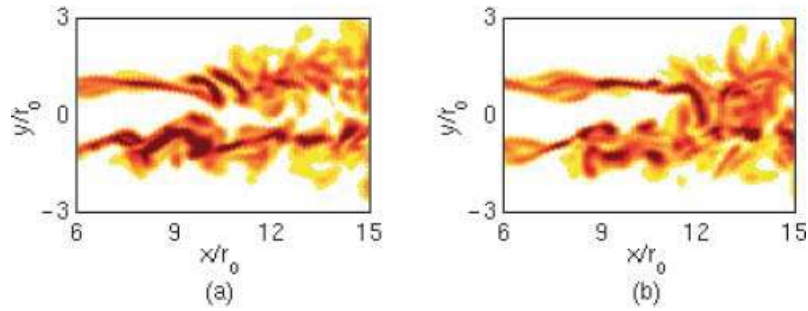
Figure 18. Snapshot of the vorticity ω in the plane $z = 0$ at times (a) $t^* = 6.2$ and (b) $t^* = 7.5$. Color scale is from 6×10^4 up to 3×10^5 m s^{-2}.
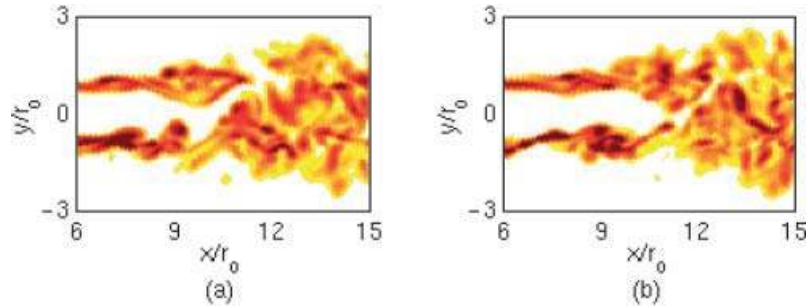

Figure 19. Snapshot of the vorticity ω in the plane $z = 0$ at times (a) $t^* = 2.2$ and (b) $t^* = 3.5$. Color scale is from 6×10^4 up to 3×10^5 m s^{-2}.
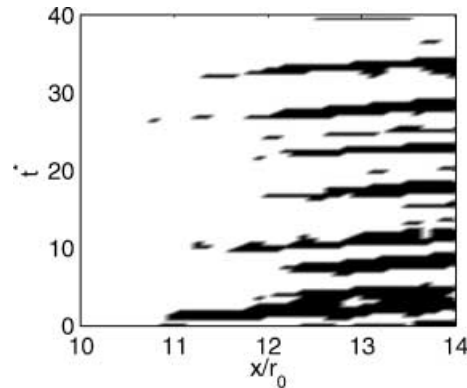

Figure 20. Space–time evolution of the distance between the shear layers δ_{sl} in the plane $z = 0$. The regions in black are for $\delta_{\mathrm{sl}} \leq 0.05 r_0$.

The time evolution of δ_{sl} for $x = 12.1 r_0$ is plotted in Figure 21. This profile is located just after the potential core, and therefore must clearly indicate the occurrence of the breakdowns of the shear layer in the region of the end of the potential core. Breakdowns are detected when δ_{sl} is equal to zero. Since eight cancellations are observed during the recording time, a Strouhal number of $St \simeq 0.2$ can be associated with these flow events. This corresponds to the Strouhal number of the predominant sound radiation for $\hat{\theta} = 30°$.

To exhibit a link between the breakdowns of the shear layer and the acoustic field, the coincidences between the negative peaks of Figure 16(a) and the cancellations of δ_{sl} at $x = 12.1 r_0$ are studied. A time delay $\Delta t_r^* = 5.3$ between the two signals is applied to deal with the propagation time. This value has been determined using the maximum wave front described in the previous subsection, by matching its negative peak with the corresponding cancellation of δ_{sl}. The correlation existing between the two signals is thus shown in Figure 22. The same periodicity is observed on both figures and the six negative pressure peaks nicely cor-
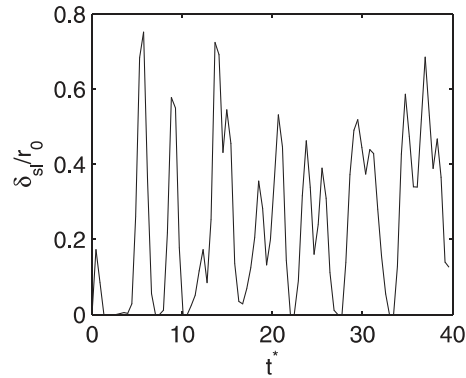
Figure 21. Time evolution of the distance δ_{sl} for $x = 12.1r_0$.
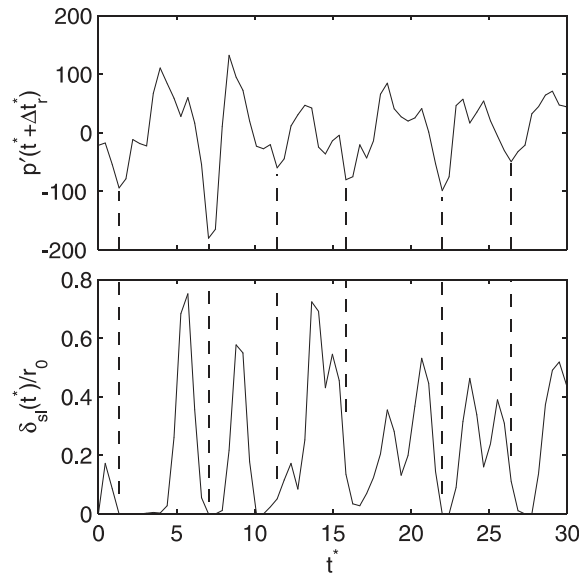

Figure 22. Time evolution of the fluctuating pressure $p'\left(t^* + \Delta t_r^*\right)$ for $x = 24.8r_0$, $y = 8r_0$ and $z = 0$, and of the distance $\delta_{sl}(t^*)$ for $x = 12.1r_0$, with the time delay $\Delta t_r^* = 5.3$.

respond to the cancellations of the distance between the shear layers. The only slight disagreement is found for the third negative pressure peak, which has, as it happens, the lowest amplitude.

This good correlation demonstrates that, for the simulated moderate Reynolds number jet, the predominant low frequency noise radiated in the downstream direction is connected to the intermittent breakdown of the shear layers in the jet at the end of the potential core. The sudden acceleration of the vortical structures when coming into the jet center region, followed by the stretching of the local shear layer, may be involved. For larger angles, the acoustic field is rather associated with more random flow events, generating broadband frequency noise. Among these sources radiating upstream, some are likely to be located in the turbulent shear layers where coherent vortical structures interact.

6. Conclusion

In this paper, a subsonic circular jet with a Mach number of 0.9 and a Reynolds number of 6.5×10^4 is computed by LES to study its radiated acoustic field. Non-dispersive schemes and non-reflecting boundary conditions developed for aeroacoustics are used to directly obtain the sound field generated by the jet.

The first feature of the present work is that both flow field and acoustic radiation provided by the simulation are systematically validated by comparison with the experimental data available in the literature. Parameters of the flow field such as the mean flow, turbulence intensities, velocity spectra and integral length scales are in very good agreement with experiments both in the turbulent transition region and the fully turbulent region of the jet. Sound pressure spectra and directivities obtained in the acoustic field agree well with corresponding experimental results, and predominant sound sources in the jet are also apparently located just after the end of the potential core, in accordance with observations. These validations demonstrate the feasibility of the direct calculation of the acoustic field generated by subsonic jets using LES. They are also essential to make sure that the noise generation mechanisms are well described in the simulation.

The second feature of the present work is an attempt to find a link between the flow field and acoustic radiation, in order to investigate the sound sources in subsonic jets. It is important because, unlike in supersonic jets where Mach waves dominate the sound field, sound sources in subsonic jets are still not clearly identified. The predominant low frequency acoustic radiation, found in the downstream direction of jets at every Reynolds number, is generally attributed to coherent flow structures. In the present study at a moderate Reynolds number, a correlation between this radiation and the breakdown of the shear layers in the jet center zone near the end of the potential core is shown. This suggests that the sudden periodic accelerations of vortical structures in this region are responsible for the predominant noise radiation. The broader band frequency noise radiated by jets for larger angles depends on the Reynolds number and is classicaly associated with the small-scale turbulence. The interactions of flow structures within the turbulent shear layers before the end of the potential core may be one of these sources, as shown by an illustration in this study. Further investigations are required to support the present observations, particularly at high Reynolds numbers where the breakdowns of the shear layer at the end of the potential core may not be the primary noise generation mechanism. It would also be interesting to study the connection between the three-dimensional structures of the jet and the sound field.

Acknowledgment

Appendix A.   Filtered Full Navier–Stokes Equations

We consider the full compressible three-dimensional Navier–Stokes equations written in conservative form in Cartesian coordinates. The fluid is considered as a perfect gas so that the total energy is $\varrho e = p/(\gamma - 1) + \varrho(u_1^2 + u_2^2 + u_3^2)/2$, where ϱ, u_1, u_2, u_3, e and p are the density, the three velocity components, the total specific energy and the pressure, respectively, and γ is the specific heat ratio. In an LES, these equations are filtered spatially. The system solved in the present study is then

$$\frac{\partial \mathbf{U}}{\partial t} + \frac{\partial \mathbf{E_e}}{\partial x_1} + \frac{\partial \mathbf{F_e}}{\partial x_2} + \frac{\partial \mathbf{G_e}}{\partial x_3} - \frac{\partial \mathbf{E_v}}{\partial x_1} - \frac{\partial \mathbf{F_v}}{\partial x_2} - \frac{\partial \mathbf{G_v}}{\partial x_3} = 0 \, ,$$

where the unknown vector is $\mathbf{U} = (\overline{\varrho}, \overline{\varrho u_1}, \overline{\varrho u_2}, \overline{\varrho u_3}, \overline{\varrho e})^t$, the overbar denoting the LES filter. For a compressible flow, it is useful to introduce Favre averaging to evaluate the computed velocity and specific total energy as $\tilde{u}_i = \overline{\varrho u_i}/\overline{\varrho}$ and $\tilde{e} = \overline{\varrho e}/\overline{\varrho}$. This density-weighted filter is denoted by a tilde. Moreover, the unresolved part of all variables are written as f''. Resolved Euler fluxes are denoted by the subscript $\mathbf{e}$, and they are given by

$$\mathbf{E_e} = \left(\overline{\varrho}\tilde{u}_1, \, \overline{p} + \overline{\varrho}\tilde{u}_1^2, \, \overline{\varrho}\tilde{u}_1\tilde{u}_2, \, \overline{\varrho}\tilde{u}_1\tilde{u}_3, \, (\overline{\varrho}\tilde{e} + \overline{p})\tilde{u}_1 \right)^t ,$$

$$\mathbf{F_e} = \left(\overline{\varrho}\tilde{u}_2, \, \overline{\varrho}\tilde{u}_1\tilde{u}_2, \, \overline{p} + \overline{\varrho}\tilde{u}_2^2, \, \overline{\varrho}\tilde{u}_2\tilde{u}_3, \, (\overline{\varrho}\tilde{e} + \overline{p})\tilde{u}_2 \right)^t ,$$

$$\mathbf{G_e} = \left(\overline{\varrho}\tilde{u}_3, \, \overline{\varrho}\tilde{u}_1\tilde{u}_3, \, \overline{\varrho}\tilde{u}_2\tilde{u}_3, \, \overline{p} + \overline{\varrho}\tilde{u}_3^2, \, (\overline{\varrho}\tilde{e} + \overline{p})\tilde{u}_3 \right)^t .$$

The terms denoted by the subscript **v** are the resolved viscous fluxes and the subgrid scale terms

$$\mathbf{E_v} = \left(0,\, \widetilde{\tau_{11}} + \mathcal{T}_{11},\, \widetilde{\tau_{12}} + \mathcal{T}_{12},\, \widetilde{\tau_{13}} + \mathcal{T}_{13},\, \widetilde{u}_i\left(\widetilde{\tau_{1i}} + \mathcal{T}_{1i}\right)\right)^t,$$

$$\mathbf{F_v} = \left(0,\, \widetilde{\tau_{21}} + \mathcal{T}_{21},\, \widetilde{\tau_{22}} + \mathcal{T}_{22},\, \widetilde{\tau_{23}} + \mathcal{T}_{23},\, \widetilde{u}_i\left(\widetilde{\tau_{2i}} + \mathcal{T}_{2i}\right)\right)^t,$$

$$\mathbf{G_v} = \left(0,\, \widetilde{\tau_{31}} + \mathcal{T}_{31},\, \widetilde{\tau_{32}} + \mathcal{T}_{32},\, \widetilde{\tau_{33}} + \mathcal{T}_{33},\, \widetilde{u}_i\left(\widetilde{\tau_{3i}} + \mathcal{T}_{3i}\right)\right)^t.$$

The viscous stress tensor $\widetilde{\tau}_{ij}$ is defined by $\widetilde{\tau}_{ij} = 2\mu\widetilde{S}_{ij}$ where μ is the dynamic molecular viscosity, and $\widetilde{S}_{ij}$ is the deviatoric part of the resolved deformation stress tensor

$$\widetilde{S}_{ij} = \frac{1}{2}\left(\frac{\partial \widetilde{u}_i}{\partial x_j} + \frac{\partial \widetilde{u}_j}{\partial x_i} - \frac{2}{3}\delta_{ij}\frac{\partial \widetilde{u}_k}{\partial x_k}\right).$$

The subgrid scale terms retained are the subgrid scale stress tensor $\mathcal{T}_{ij}$ in the momentum equations and $u_j\mathcal{T}_{ij}$ in the energy equations. The first one appears naturally as

$$\mathcal{T}_{ij} = -\overline{\varrho}\widetilde{u_i u_j} + \overline{\varrho}\widetilde{u}_i\widetilde{u}_j \simeq -\overline{\varrho}\widetilde{u_i'' u_j''}.$$

The second one comes from the term $-\overline{\varrho}\widetilde{eu_j} + \overline{\varrho}\,\widetilde{e}\widetilde{u}_j$ which can be simplified as

$$-\overline{\varrho}\widetilde{eu_j} + \overline{\varrho}\,\widetilde{e}\widetilde{u}_j \simeq -\overline{\varrho}\widetilde{u_i'' u_j'' u_i''} \simeq \mathcal{T}_{ij}\widetilde{u}_i''.$$

To evaluate the subgrid scale stress tensor from the resolved scales, the classical strategy consists of reproducing the dissipative effects of the unresolved scales through the model (see the review of Lesieur and Métais (1996) for instance). The subgrid scale tensor can then be modeled by

$$\mathcal{T}_{ij} = 2\mu_t\widetilde{S}_{ij} - \frac{2}{3}\overline{\varrho}k_{\text{sgs}}\delta_{ij},$$

where μ_t is the turbulent viscosity and k_{sgs} is the subgrid scale energy. In the present study, the latter is neglected because it is very small compared with the thermodynamic pressure, as shown by Erlebacher *et al.* (1992), and because the major part of the turbulent energy is resolved. The turbulent viscosity is estimated using the model of Smagorinsky (1963), and is assumed to be proportional to a subgrid characteristic length scale and to a characteristic turbulent velocity

$$\mu_t = \overline{\varrho}\,(C_s\Delta_c)^2\sqrt{2\widetilde{S}_{ij}\,\widetilde{S}_{ij}},$$

where C_s is the Smagorinsky constant, and Δ_c is usually given by $\Delta_c = \sqrt[3]{\Delta x_1 \Delta x_2 \Delta x_3}$. By assuming that the cut-off wave number, typically π/Δ_c, lies in the inertial zone of the turbulence, μ_t is determined to provide the dissipation of the energy transferred from the resolved to the unresolved scales in isotropic turbulence, yielding $C_s = 0.18$.

Appendix B. Formulation of boundary conditions

At the inflow and at the lateral sides of the computational domain, radiation boundary conditions are applied. They are given by the differential system governing the behavior of acoustic perturbations in the far field, and they are written, in spherical coordinates (r, θ, φ), as

$$\frac{\partial}{\partial t}\begin{pmatrix} \varrho \\ u_i \\ p \end{pmatrix} + v_g\left(\frac{\partial}{\partial r} + \frac{1}{r}\right)\begin{pmatrix} \varrho - \varrho_0 \\ u_i - u_{i0} \\ p - p_0 \end{pmatrix} = 0 \qquad \text{for} \quad i = 1, 2, 3,$$

where v_g is the acoustic group velocity, and ϱ_0, u_{i0} and p_0 are the mean density, velocity components and pressure, respectively. These mean quantities are computed during the simulation and converge rapidly to steady values. The mean sound speed is then evaluated as $c_0 = \sqrt{\gamma p_0/\varrho_0}$.

The outflow conditions are obtained by modifying the previous equations to enable the exit of vortical or entropic perturbations, and they are written as

$$\frac{\partial \varrho}{\partial t} + \mathbf{u}_0 \cdot \nabla (\varrho - \varrho_0) \quad = \frac{1}{c_0^2} \left(\frac{\partial p}{\partial t} + \mathbf{u}_0 \cdot \nabla (p - p_0) \right) ,$$

$$\frac{\partial u_i}{\partial t} + \mathbf{u}_0 \cdot \nabla (u_i - u_{i0}) \quad = -\frac{1}{\varrho_0} \frac{\partial (p - p_0)}{\partial x_i} \quad \text{for} \quad i = 1, 2, 3 ,$$

$$\frac{\partial p}{\partial t} + v_\mathrm{g} \left(\frac{\partial}{\partial r} + \frac{1}{r} \right) (p - p_0) = 0 .$$

The accuracy of these boundary conditions has been estimated with two test cases in Bogey (2000) and in Bogey and Bailly (2002). The first case, dealing with the propagation of an acoustical pulse, has demonstrated that acoustic disturbances leave the computational domain without significant reflection. The second one, consisting of the convection of a vortex ring, has shown that the exit of a vortical structure generates spurious waves which are small with respect to the aerodynamic field, but might not be negligible in comparison with the low-amplitude physical sound field.

Appendix C. Inflow Forcing

In jet simulations it is necessary to introduce small disturbances near the inflow to seed the turbulence and allow laminar–turbulent transition. Natural flow development is obtained with a random forcing and the classical method consists in adding a synthetic turbulent field to the mean flow. In the present study, to minimize the production of spurious acoustic waves by the forcing, velocity fluctuations are only introduced into the shear layers of the jet, and they are divergence-free. A vortex ring of radius r_0 is therefore considered, with an axial velocity Ux_0 and a radial velocity Ur_0 given by

$$Ux_0 = 2 \, \frac{r_0}{r} \, \frac{r - r_0}{\Delta_0} \, \exp \left(-\ln(2) \, \left(\frac{\Delta(x,r)}{\Delta_0} \right)^2 \right) ,$$

$$Ur_0 = -2 \, \frac{r_0}{r} \, \frac{x - x_0}{\Delta_0} \, \exp \left(-\ln(2) \, \left(\frac{\Delta(x,r)}{\Delta_0} \right)^2 \right)$$

for $r = \sqrt{y^2 + z^2} \neq 0$, where $\Delta(x, r)^2 = (x - x_0)^2 + (r - r_0)^2$ and $x_0 = 0.8 r_0$. The vortex has no azimuthal velocity, and the vortex velocity reaches a maximum value of 1 for $\Delta(x, r) = \Delta_0$. The excitation is built up by combining the basic vortex ring with the azimuthal functions $\cos(n\theta)$ for $n = 0, \dots, 9$. Disturbances are thus superimposed on the jet flow at every iteration in the following way:

$$u_x = u_x + \sum_{n=0}^{9} \alpha \varepsilon_n \, \cos(n\theta + \varphi_n) Ux_0 U_j ,$$

$$u_r = u_r + \sum_{n=0}^{9} \alpha \varepsilon_n \, \cos(n\theta + \varphi_n) Ur_0 U_j ,$$

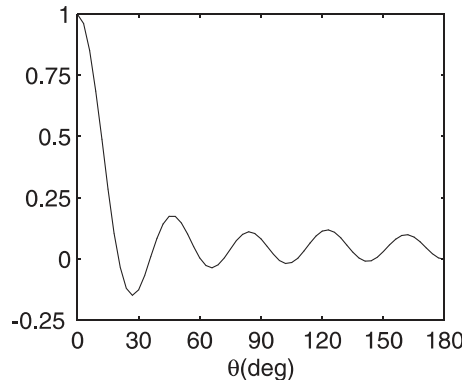**Figure 23.** Azimuthal cross correlation function of the axial velocity disturbances superimposed on the jet flow by the excitation.

where ε_n and φ_n are uniform random variables in time, between -1 and 1, and between 0 and 2π, respectively. The variables ε_n and φ_n correspond to the random amplitudes and phases of each forcing mode, and they are updated at each iteration. The frequency spectrum of the excitation disturbances is very broad, and a large part of the spectrum, wider than the grid can resolve, is rapidly damped. The amplitude α is taken as 0.01, so that the turbulence intensities generated by the forcing are around 4%, of the order of experimental values. Furthermore, to check that the excitation is random not only in time, but also in space, the azimuthal correlation function of the forcing axial velocity is presented in Figure 23. The forcing disturbances are not correlated azimuthally for angles higher than 20°. The excitation is thus sufficiently stochastic for modeling the jet inflow conditions.

References

Bailly, C., and Juvé, D. (2000). Numerical solution of acoustic propagation problems using linearized Euler equations. *AIAA J.*, **38**(1), 22–29.

Bailly, C., Lafon, P., and Candel, S. (1997). Subsonic and supersonic jet noise prediction from statistical source models. *AIAA J.*, **35**(11), 1688–1696.

Bastin, F., Lafon, P., and Candel, S. (1997). Computation of jet mixing noise due to coherent structures: the plane jet case. *J. Fluid Mech.*, **335**, 261–304.

Boersma, B.J., Brethouwer, G., and Nieuwstadt, F.T.M. (1998). A numerical investigation on the effect of the inflow conditions on a self-similar region of a round jet. *Phys. Fluids*, **10**(4), 899–909.

Bogey, C. (2000). Calcul direct du bruit aérodynamique et validation de modèles acoustiques hybrides. Ph.D. Thesis of Ecole Centrale de Lyon, No. 2000-11.

Bogey, C., and Bailly, C (2002). Three-dimensional non-reflective boundary conditions for acoustic simulations: far field formulation and validation test cases. *Acta Acustica*, **88**, 463–471.

Bogey, C., Bailly, C., and Juvé, D. (2000). Numerical simulation of the sound generated by vortex pairing in a mixing layer. *AIAA J.*, **38**(12), 2210–2218.

Bogey, C., Bailly, C., and Juvé, D. (2002). Computation of flow noise using source terms in linearized Euler's equations. *AIAA J.*, **40**(2), 235–243.

Bridges, J., and Hussain, F. (1992). Direct evaluation of aeroacoustic theory in a jet. *J. Fluid Mech.*, **240**, 469–501.

Brown, G.L., and Roshko, A. (1974). On density effects and large structure in turbulent mixing layers. *J. Fluid Mech.*, **64**(4), 775–816.

Chu, W.T., and Kaplan, R.E. (1976). Use of a spherical concave reflector for jet-noise-source distribution diagnosis. *J. Acous. Soc. Am.*, **59**(6), 1268–1277.

Colonius, T., Lele, S.K., and Moin, P. (1993). Boundary conditions for direct computation of aerodynamic sound generation. *AIAA J.*, **31**(9), 1574–1582.

Constantinescu, G.S., and Lele, S. (2001). Large eddy simulation of a near sonic turbulent jet and its radiated noise. AIAA Paper No. 2001-0376.

Davies, P.O.A.L, Fisher, M.J., and Barrat, M.J. (1963). Turbulence in the mixing region of a round jet. *J. Fluid Mech.*, **15**, 337–367.

Erlebacher, G., Hussaini, M.Y., Speziale, C.G., and Zang, T.A. (1992). Toward the large-eddy simulation of compressible turbulent flows. *J. Fluid Mech.*, **238**, 155–185.

Freund, J.B. (2001). Noise sources in a low-Reynolds-number turbulent jet at Mach 0.9. *J. Fluid Mech.*, **438**, 277–305.

Freund, J.B., Lele, S.K., and Moin, P. (2000). Numerical simulation of a Mach 1.92 turbulent jet and its sound field. *AIAA J.*, **38**(11), 2023–2031.

Gamet, L., and Estivalezes, J.L. (1998). Application of LES and Kirchhoff method to jet noise prediction. *AIAA J.*, **36**(12), 2170–2178.

Hussain, A.K.M.F. (1986). Coherent structures and turbulence. *J. Fluid Mech.*, **173**, 303–356.

Hussein, H.J., Capp, S.P., and George, W.K. (1994). Velocity measurements in a high-Reynolds-number, momentum-conserving, axisymmetric, turbulent jet. *J. Fluid Mech.*, **258**, 31–75.

Juvé, D., Sunyach, M., and Comte-Bellot, G. (1980). Intermittency of the noise emission in subsonic cold jets. *J. Sound. Vib.*, **71**(3), 319–332.

Kibens, V. (1980). Discrete noise spectrum generated by an acoustically excited jet. *AIAA J.*, **18**(4), 434–441.

Lau, J.C., Morris, P.J., and Fisher, M.J. (1979). Measurements in subsonic and supersonic free jets using a laser velocimeter. *J. Fluid Mech.*, **93**(1), 1–27.

Laufer, J., Kaplan, R.E., and Chu, W.T. (1974). On the generation of jet noise. AGARD CP-131 on Noise mechanism.

Lesieur, M., and Métais, O. (1996). New trends in large-eddy simulations of turbulence. *Annu. Rev. Fluid Mech.*, **28**, 45–82.

Lighthill, M.J. (1952). On sound generated aerodynamically – I. General theory. *Proc. Ro. Soc. London*, Ser. A, **211**, 564–587.

Lilley, G.M. (1972). The generation and radiation of supersonic jet noise. Vol. IV – Theory of turbulence generated jet noise, noise radiation from upstream sources, and combustion noise. Part II: Generation of sound in a mixing region. AFAPL-TR-72-53, Vol. IV, Air Force Aero Propulsion Laboratory.

Lilley, G.M. (1994). Jet noise classical theory and experiments. In *Aeroacoustics of Flight Vehicles*, Vol. 1 (H.H. Hubbard, ed.), Publisher: Acoustical Society of America, pp. 211–289.

Lilley, G.M. (1996). The radiated noise from isotropic turbulence with application to the theory of jet noise. *J. Sound. Vib.*, **190**(3), 463–476.

Long, D.F., and Arndt, R.E.A. (1984). Jet noise at low Reynolds number. *AIAA J.*, **22**(2), 187–193.

Lush, P.A. (1971). Measurements of subsonic jet noise and comparison with theory. *J. Fluid Mech.*, **46**(3), 477–500.

Michalke, A. (1965). On spatially growing disturbances in an inviscid shear layer. *J. Fluid Mech.*, **23**, 521–544.

Mollo-Christensen, E., Kolpin, M.A., and Martucelli, J.R. (1964). Experiments on jet flows and jet noise far-field spectra and directivity patterns. *J. Fluid Mech.*, **18**, 285–301.

Morris, P.J., Long, L.N., and Scheidegger, T.E. (1999). Parallel computations of high speed jet noise. AIAA Paper No. 99-1873.

Panchapakesan, N.R., and Lumley, J.L. (1993). Turbulence measurements in axisymmetric jets of air and helium. Part I. Air jet. *J. Fluid Mech.*, **246**, 197–223.

Ribner, H.S. (1964). The generation of sound by turbulent jets. In *Advances in Applied Mechanics*, Vol. VIII, pp. 103–182. Academic Press, New-York.

Ricou, F.P., and Spalding, D.B. (1961). Measurements of entrainment by axisymmetrical turbulent jets. *J. Fluid Mech.*, **11**, 21–32.

Schaffar, M. (1979). Direct measurements of the correlation between axial in-jet velocity fluctuations and far field noise near the axis of a cold jet. *J. Sound. Vib.*, **64**(1), 73–83.

Shen, H., and Tam, C.K.W. (1998). Numerical simulation of the generation of the axisymmetric mode jet screech tones. *AIAA J.*, **36**(10), 1801–1807.

Smagorinsky, J.S. (1963). General circulation experiments with the primitive equations: I. The basic experiment. *Mon. Weath. Rev.* **91**, 99–163.

Stromberg, J.L., McLaughlin, D.K., and Troutt, T.R. (1980). Flow field and acoustic properties of a Mach number 0.9 jet at a low Reynolds number. *J. Sound. Vib.*, **72**(2), 159–176.

Tam, C.K.W. (1995a). Supersonic jet noise. *Annu. Rev. Fluid Mech.*, **27**, 17–43.

Tam, C.K.W. (1995b). Computational aeroacoustics: issues and methods. *AIAA J.*, **33**(10), 1788–1796.

Tam, C.K.W. (1998). Jet noise: since 1952. *Theoret. Comput. Fluid Dynamics*, **10**, 393–405.

Tam, C.K.W., and Burton, D.E. (1984). Sound generated by instability waves of supersonic flows. Part 2: axisymmetric jets. *J. Fluid Mech.*, **138**, 273–295.

Tam, C.K.W., and Dong, Z. (1996). Radiation and outflow boundary conditions for direct computation of acoustic and flow disturbances in a nonuniform mean flow. *J. Comput. Acoust.*, **4**(2), 175–201.

Tam, C.K.W., and Webb, J.C. (1993). Dispersion-relation-preserving finite difference schemes for computational acoustics. *J. Comput. Phys.*, **107**, 262–281.

Troutt, T.R., and McLaughlin, D.K. (1982). Experiments on the flow and acoustic properties of a moderate-Reynolds-number supersonic jet. *J. Fluid Mech.*, **116**, 123–156.

Winant, C.D., and Browand, F.K. (1974). Vortex pairing: the mechanism of turbulent mixing-layer growth at moderate Reynolds number. *J. Fluid Mech.*, **63**(2), 237–255.

Wygnanski, I., and Fiedler, H. (1969). Some measurements in the self-preserving jet. *J. Fluid Mech.*, **38**(3), 577–612.

Zaman, K.B.M.Q. (1985). Far-field noise of a subsonic jet under controlled excitation. *J. Fluid Mech.*, **152**, 83–111.

Zhao, W., Frankel, S.H., and Mongeau, L. (2001). Large eddy simulations of sound radiation from subsonic turbulent jets. *AIAA J.*, **39**(8), 1469–1477.